FULL PAPER

ADVANCED
FUNCTIONAL
MATERIALS

Type-II Dirac Semimetals

www.afm-journal.de

Low-Temperature Eutectic Synthesis of PtTe$_2$ with Weak Antilocalization and Controlled Layer Thinning

Song Hao, Junwen Zeng, Tao Xu, Xin Cong, Chenyu Wang, Chenchen Wu, Yaojia Wang, Xiaowei Liu, Tianjun Cao, Guangxu Su, Lanxin Jia, Zhangting Wu, Qian Lin, Lili Zhang, Shengnan Yan, Mengfan Guo, Zhenlin Wang, Pingheng Tan, Litao Sun, Zhenhua Ni, Shi-Jun Liang,* Xinyi Cui, and Feng Miao*

Metallic transition metal dichalcogenides (TMDs) have exhibited various exotic physical properties and hold the promise of novel optoelectronic and topological devices applications. However, the synthesis of metallic TMDs is based on gas-phase methods and requires high-temperature condition. As an alternative to the gas-phase synthetic approach, lower temperature eutectic liquid-phase synthesis presents a very promising approach with the potential for larger-scale and controllable growth of high-quality thin metallic TMD single crystals. Here, the first realization of low-temperature eutectic liquid-phase synthesis of type-II Dirac semimetal PtTe$_2$ single crystals with thickness ranging from 2 to 200 nm is presented. The electrical measurement of synthesized PtTe$_2$ reveals a record-high conductivity of as high as 3.3×10^6 S m^{-1} at room temperature. Besides, the weak antilocalization behavior is identified experimentally in the type-II Dirac semimetal PtTe$_2$ for the first time. Furthermore, a simple and general strategy is developed to obtain atomically thin PtTe$_2$ crystal by thinning as-synthesized bulk samples, which can still retain highly crystalline and exhibits excellent electrical conductivity. The results of controllable and scalable low-temperature eutectic liquid-phase synthesis and layer-by-layer thinning of high-quality thin PtTe$_2$ single crystals offer a simple and general approach for obtaining different thickness metallic TMDs with high melting-point transition metal.

1. Introduction

2D semiconducting transition metal dichalcogenides (TMDs) materials have been widely studied for promising applications in electronic, optoelectronic and spintronic devices.[1–6] Beyond semiconducting TMDs, metallic TMD materials with exotic properties have also attracted much attention over the past few years.[7–13] However, synthesis and properties of metallic TMD materials remain less unexplored compared with well-studied semiconducting TMDs, although they show enormous potential applications, such as improving contact properties of 2D semiconductor transistors[14,15] and enhancing catalysis performances.[16–19]

Recently, platinum tellurium (PtTe$_2$) has been identified as a type-II Dirac semimetal through angle-resolved photoemission spectroscopy (ARPES),[20] which opens a new door to investigate various intriguing physical properties of metallic TMDs. In stark contrast to graphene (known as type-I Dirac semimetal), PtTe$_2$ has a tilted Dirac cone with linear

Dr. S. Hao, J. W. Zeng, C. Y. Wang, C. C. Wu, Y. J. Wang, X. W. Liu,
T. J. Cao, G. X. Su, L. X. Jia, L. L. Zhang, S. N. Yan, Prof. Z. L. Wang,
Dr. S.-J. Liang, Prof. F. Miao
National Laboratory of Solid State Microstructures
School of Physics
Collaborative Innovation Center of Advanced Microstructures
Nanjing University
Nanjing 210093, China
E-mail: sjliang@nju.edu.cn; miao@nju.edu.cn
Dr. T. Xu, Prof. L. T. Sun
SEU-FEI Nano-Pico Center
Key Laboratory of MEMS of Ministry of Education
Southeast University
Nanjing 210096, China

The ORCID identification number(s) for the author(s) of this article can be found under https://doi.org/10.1002/adfm.201803746.

X. Cong, Prof. P. H. Tan
State Key Laboratory of Superlattices and Microstructures
Institute of Semiconductors
Chinese Academy of Sciences
Beijing 100083, China
Dr. Z. T. Wu, Q. Lin, Prof. Z. H. Ni
School of Physics
Southeast University
Nanjing 211189, China
M. F. Guo, Prof. X. Y. Cui
State Key Laboratory of Pollution Control and Resource Reuse
School of the Environment
Nanjing University
Nanjing 210046, China

1803746 (1 of 9)

dispersion. The titled Dirac cone at certain momentum direction may provide a new platform to investigate anisotropic magneto-transport properties, similar to type-II Weyl semimetals.[21–24] According to ARPES and theoretical results,[20] the Dirac cone is buried in the valence band and Te-p orbitals are responsible for formation of valence bands. The overlap repulsion between filled 5p orbitals of Te is much stronger in each Te-atom sheet than adjacent two Te-atom sheets, creating an ultra-strong covalent bonds joining adjacent layers.[25] The strong interlayer interactions in $PtTe_2$ would lead to many interesting thickness-dependent electronic properties.[26–29] The $PtTe_2$ with different thicknesses can be accessed either by direct chemical vapor deposition (CVD) or layer-by-layer thinning approach. In particular for the controlled layer thinning approach, it is very promising to be a simple, general and nondestructive strategy to achieve metallic TMDs with strong interlayer interactions. Besides, the heavy Pt and Te atoms in type-II Dirac semimetal $PtTe_2$ lead to a strong spin-orbital interaction, which enables the occurence of weak antilocalization. To investigate these peculiar physical properties, it is highly desirable to synthesize high-quality stoichiometric $PtTe_2$ single crystals with different thicknesses through a simple and general approach.

Up to now, chemical vapor transport (CVT) and CVD techniques are mostly used methods to synthesize single crystals. However, CVT-synthesized samples often encounter nonstoichiometric issues.[27,30] Moreover, the strong interlayer interactions would lead to a challenge in obtaining atomically thin crystals through mechanical exfoliation of CVT-synthesized samples,[25–27] or through direct CVD method, which drastically affects the studies of fundamental properties and potential topological device applications of $PtTe_2$ thin crystals. Even worse, both CVT and CVD techniques require high-temperature sublimation of precursors to synthesize the metallic TMDs with high melting-point transition metal. From the viewpoint of thermodynamics, it is noteworthy that elements Pt and Te can form eutectic solution and yield $PtTe_x$ compounds with various stoichiometric ratio, dependent on reaction temperature and atomic ratio of precursors.[31] Therefore, it is quite promising to develop a low-temperature synthesis of stoichiometric and high-quality thin $PtTe_2$ single crystals through the facile eutectic solidification, which can be used to uncover the weak antilocalization phenomenon in type-II Dirac semimetals.

In this work, we report the first low-temperature eutectic liquid-phase synthesis of large scale $PtTe_2$ single crystals with thickness ranging from 2 to 200 nm by utilizing a novel solid–liquid–solid (SLS) approach. Electrical measurement of $PtTe_2$ four-terminal Hall-bar devices reveals an ultrahigh electrical conductivity of 3.3×10^6 S m^{-1} at room temperature, which is a record high among metallic TMDs reported so far. We also experimentally identify the weak antilocalization in type-II Dirac semimetals. Furthermore, we develop a simple and general layer-by-layer thinning method to obtain atomically thin $PtTe_2$ crystal, which can retain the excellent electric conductivity similar to as-grown samples.

2. Results and Discussion

We synthesized $PtTe_2$ on amorphous SiO_2/Si substrates in a CVD-like furnace through a novel and facile eutectic solidification method, as shown in **Figure 1**a. Due to lower vapor pressure of PtO_2 and lower reaction activity of $PtCl_2$, we selected elemental Pt as the reactant precursor and SiO_2/Si as substrate, which is different from previous works of using powdered reactant as precursors to synthesize metallic TMDs on mica substrate.[10,15] Based on phase diagram of Pt–Te system (see Figure S1 in the Supporting Information), we design a programing temperature of furnace as shown in Figure 1b[31] and demonstrate the whole growth processes in Figure 1c. The principle of chemical reaction is based on the Pt–Te eutectic solidification. According to the phase diagram (see Figure S1, Supporting Information), the excess Te powders can react with Pt to produce the pure phase $PtTe_2$. The reaction process can be described in the following way. When temperature is close to 400 °C, as-deposited Pt films covered with Te powders would gradually dissolve into excess liquid Te, which results in formation of Pt–Te solid solution. As the reaction temperature continues to increase, excess liquid Te would be evaporated and carried by carrier gas to downstream, providing a Te-rich atmosphere to prevent as-grown crystals from oxidation. Eventually, the crystals are formed after nucleation and growth, followed by lateral and vertical competitive expansion of crystalline domains. By analogy with vapor–liquid–solid growth mechanism for semiconducting nanowires, the solid-liquid-solid (SLS) growth is proposed to account for the growth mechanism, in which the whole reaction proceeds continuously from Pt–Te solid, liquid, to solid.[32] In the synthesis of $PtTe_2$ single crystals, Te not only serves as reactant precursor but also lowers the melting point of elemental Pt through forming eutectic system similar to prior works where tellurium also severs as a flux and is removed by the Ar/H$_2$ flow finally.[33,34] Note that the term CVD is not strictly suitable for the chemical reaction described above because precursors react in a molten solution rather than in the vapor phase.[35–37]

Based on the SLS growth mechanism, as-synthesized samples display either hexagonal or triangle shape (see Figure 1d), with lateral size of several tens of micrometers. The uniform color contrast both for hexagonal and triangular $PtTe_2$ single crystals indicates relatively high quality of as-grown samples. It is noteworthy that a sea of small particles observed in the left area of optical microscopy image can be ascribed to Pt–Te byproducts under facile growth conditions. The good separation of small particles with $PtTe_2$ single crystals ensures the investigation of physical property of pure-phase $PtTe_2$ single crystals (see Figure S2 in the Supporting Information). To identify chemical elements and analyze atomic ratio of as-grown samples, we carried out elemental mapping using energy-dispersive X-ray spectroscopy (EDS) over the whole region of $PtTe_2$ single crystal (see Figure 1e). EDS mappings of Pt and Te (see Figure 1f,g) confirm the uniform distribution of Pt and Te elements in $PtTe_2$, which is consistent with optical microscopy result. The atomic ratio of Pt to Te determined by EDS spectrum (see Figure 1k) is ≈1:1.95, fairly close to its nominal stoichiometry. The X-ray photoelectron spectroscopy (XPS) survey spectrum (see Figure 1i) shows the predominant signals of Pt and Te elements. Pt 4f and Te 3d narrow scans in XPS spectra (see Figure 1j,k) exhibit characteristic subpeaks centered at ≈75.6 and ≈72.3 eV below Fermi level, assigned to doublet Pt $4f_{5/2}$ and $4f_{7/2}$ of $PtTe_2$. Based on optical microscopy result, the peaks located at ≈583.6
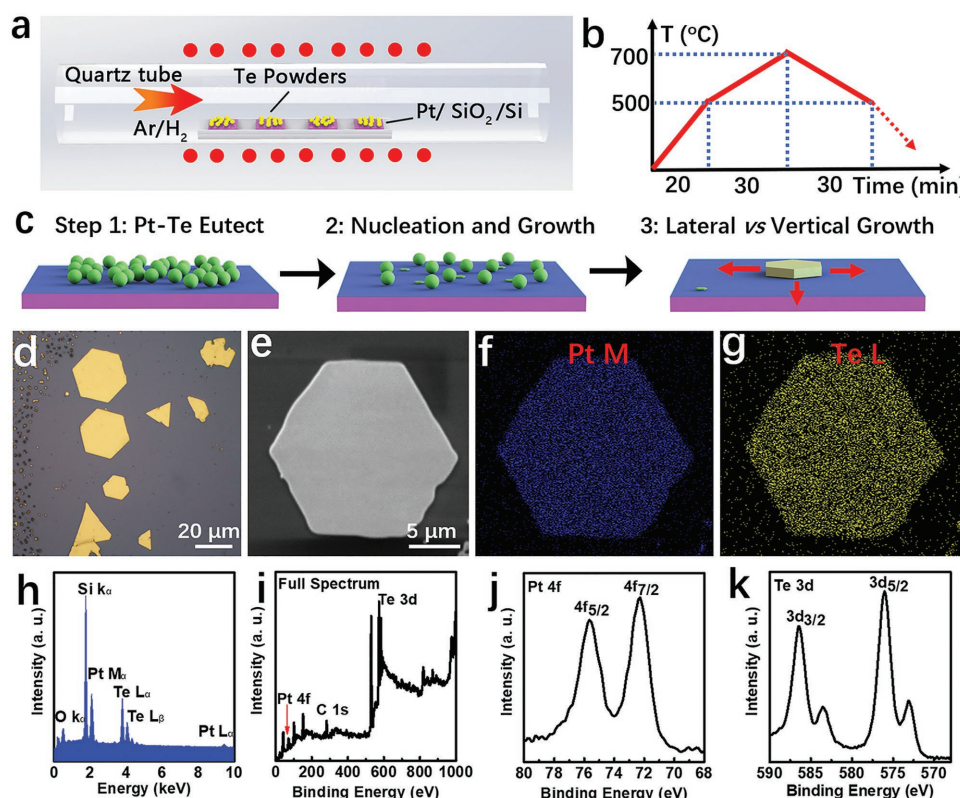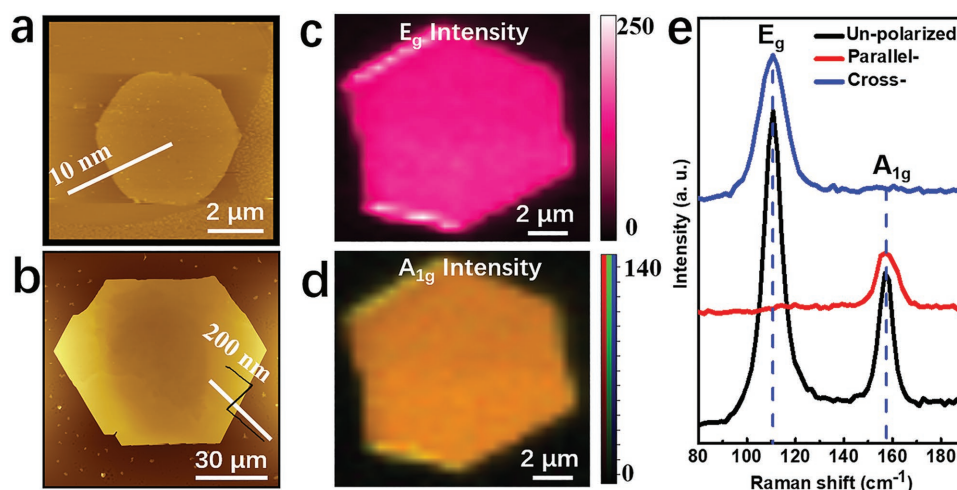
Figure 1. Direct synthesis of $PtTe_2$ single crystals on SiO_2/Si substrate in an atmospheric-pressure CVD-like furnace. a) A schematic diagram of CVD-like system. The corresponding locations of Te powders and Pt/SiO_2/Si substrates are marked. b) Temperature programming processes of Te powders. c) Schematic flow chart of the formation of $PtTe_2$ single crystals. Pt films can be slightly dissolved into Te when exceeding melting point of Te, then Pt-Te eutectic undergoes a nucleation and growth processes, yielding $PtTe_2$ single crystals. d) The optical microscopy image of typical hexagon and triangle shape $PtTe_2$ single crystals. e–h) The SEM and corresponding EDS mapping images of Pt and Te and elemental analysis of the hexagonal $PtTe_2$ flake. i–k) The corresponding XPS spectra of representative sample.

and ≈573.1 eV are assigned to Te $3d_{3/2}$ and $3d_{5/2}$ of $PtTe_2$, in accordance with previous results.[19] To investigate whether the as-grown samples are pure phase $PtTe_2$ or mixed phase of $PtTe_2$ and Pt_2Te_3, we carried out the X-ray diffraction (XRD) experiment on one of as-grown hexagonal samples, with results shown in Figure S3 (see the Supporting Information). Peaks appearing in 7.84°, 19.57°, 33.66°, and 39.35° correspond to (001), (102), (203), and (213) of $PtTe_2$ (JCPDS card No.18-0977), respectively. The other two peaks at 13.00° and 37.14° can be well indexed to (111) and (422) silicon from substrate (JCPDS card No.27-1402), respectively. The results clearly show the high purity of hexagonal $PtTe_2$ single crystals. To further confirm the $PtTe_2$ pure phase of as-grown samples, we performed additional XRD measurements of as-grown samples on other Si substrates (label as sample 1, sample 2, and sample 3) and different areas on same Si substrates (label as sample -1, sample -2, and sample -3), with results shown in Figure S4 (see the Supporting Information). A number of peaks (marked by five-pointed star) in the XRD patterns can be well-indexed to $PtTe_2$ (JCPDS card No.18-0977) and the other two peaks marked by asterisk are assigned to silicon. Note that the peaks associated with Pt_2Te_3 are not observed in the XRD patterns. Considering all these evidences above, we conclude that the excess Te powders can react with Pt to produce pure phase $PtTe_2$, instead of co-existence of $PtTe_2$ and Pt_2Te_3.

To obtain information about thickness, lateral size, and structure of as-grown samples, we performed measurements of AFM and Raman spectroscopy/Mapping. **Figure 2**a,b exhibits two hexagonal $PtTe_2$ single crystals of different lateral sizes, corresponding to thicknesses of ≈10 and ≈200 nm, respectively. It should be emphasized that atomically thin $PtTe_2$ single crystals with lateral size of several hundred nanometers can also be achieved, which is comparable to that of CVD-grown $PtSe_2$ single crystal,[27] by reducing the thickness of pre-deposited Pt films and shortening the growth time (see Figure S5 in the Supporting Information). It has been suggested that vdW growth on mica substrate for non-layered $Pb_{1-x}Sn_xSe$ and layered VSe_2 with strong interlayer interactions via a CVD method is of crucial importance to the thickness control, owing to stronger interaction between crystals and substrate.[15,38] In this work, we have used various substrates including sapphire, glass, and mica for growth of $PtTe_2$ single crystals. However, we find that the thicknesses of as-synthesized $PtTe_2$ single crystals are similar to those on SiO_2/Si substrate, indicating that the interlayer interactions of $PtTe_2$ are much stronger than that of the other materials.

Consistent with structure of CdI_2-type, synthesized sample shows Raman modes E_g and A_{1g} (see Figure 2c,d).[39] The intensity mappings show a high uniform contrast except for edges, indicative of high quality crystal. To investigate

**ADVANCED
SCIENCE NEWS**

www.advancedsciencenews.com

**ADVANCED
FUNCTIONAL
MATERIALS**

www.afm-journal.de

Figure 2. a,b) The AFM topography images of typical samples with different thicknesses. The inserted height profiles in (a) and (b) are taken along the white solid lines. c,d) Raman intensity mappings of E_g and A_{1g} characteristic modes for $PtTe_2$ sample. e) Raman spectra measured at angle of 0° under un-, parallel, and cross-polarized configurations.

polarization-dependent properties, we measured the Raman spectra of $PtTe_2$ under unpolarized and parallel-polarized as well as cross-polarized configurations in Figure 2e. There are two Raman-active modes positioned at ≈110.7 and ≈157.2 cm^{-1}, corresponding to E_g and A_{1g} modes.[9] As displayed in Figure 2e and Figure S6 (Supporting Information), the E_g (A_{1g}) mode vanishes with polarization angle α varying from 0° to 180° under parallel (cross) polarization configuration, while the A_{1g} (E_g) mode remains unchanged. These distinctive features indicate polarization-dependent anisotropic behavior of as-grown $PtTe_2$.[40,41] In addition to the polarization dependence of modes, temperature variation can shift the peaks of A_{1g} and E_g. The temperature-dependent softening modes of $PtTe_2$ (see Figure S7 in the Supporting Information) is due to anharmonic contributions induced by phonon–phonon interactions.[42–45]

Identification of the crystallinity and phase structure of as-grown $PtTe_2$ flakes is essential to reveal their unique physical properties. **Figure 3**a,b shows low-magnification transmission electron microscopy (TEM) images of typical hexagonal and triangular $PtTe_2$ crystals, respectively. To identify the crystallinity of the as-synthesized $PtTe_2$ flakes, a series of selected area electron diffraction (SAED) patterns at six different areas labeled with numbers 1–6 (see Figure 3c,d) were collected from the regular hexagonal- and triangle-shape $PtTe_2$. The angle deviation of less than 0.5° in all SAED patterns provides a solid proof of single crystallinity of SLS-synthesized $PtTe_2$ flakes. Compared to previous works that sulfurization or selenization of pre-deposited metals films on substrates yield TMD polycrystalline films,[28,46] our developed SLS approach based on a CVD-like setup can simply and rapidly synthesize high-quality TMD single crystals. $PtTe_2$ as a typical CdI_2-type structure consists of one central Pt and six Te atoms located at octahedral points (see Figure 3e where green and brown balls stand for Pt and Te atoms, respectively). Bulk $PtTe_2$ can be viewed as the AA Bernal stacking of monolayer $PtTe_2$ (see Figure 3f). The most striking feature of $PtTe_2$ is that the vdW gap (2.5 Å) is smaller than the intrinsic layer thickness (2.7 Å), in sharp contrast to the other 2D materials.[25,39] Such a smaller vdW gap indicates

abnormally strong interlayer interactions, which yields relative thick $PtTe_2$ flakes in our SLS synthesis process.

To resolve the specific structure at atomic scale, we show atomic-resolution images in Figure 3i, by zooming in the area highlighted by red rectangle in Figure 3h. The alternative bright and dark atomic arrangement (Figure 3i) in the triangular lattice suggests that the as-synthesized $PtTe_2$ preserves the 1T stacking, where the bright and dark columns are Pt and Te atom chains, respectively. Based on the intensity line profile (see Figure 3j) along the red solid line in Figure 3i, the in-plane lattice constant (a) of our as-synthesized $PtTe_2$ is estimated to be 0.39 nm, in excellent agreement with the previous report.[47]

As one of type-II Dirac semimetals, $PtTe_2$ is supposed to own excellent electrical properties. We fabricated $PtTe_2$ Hall bar devices (see **Figure 4**a) and performed measurement of resistivity at various temperatures (see Figure 4b) to reveal the electronic state property of $PtTe_2$. Similar to graphene, resistivity decreasing with temperature shows a metallic state. The measured carrier concentration of $PtTe_2$ single crystal is around 6.3×10^{22} cm^{-3} at room temperature (see Figure 4c), in accordance with its metallic property. Surprisingly, the measurement of I–V characteristic shows that the corresponding four-terminal conductivity σ_{xx} of $PtTe_2$ Hall bar devices can be 3.3×10^6 S m^{-1} at room temperature (see Figure 4d), which is a record high among 2D metallic materials reported so far.[10] To highlight the electrical conductivity of $PtTe_2$, we listed electrical conductivity of other 2D metallic materials and conventional electrode-used metals in **Table 1**. The value of electrical conductivity of as-grown $PtTe_2$ is superior to the state-of-the-art 2D metallic material VSe_2 (1.1×10^6 S m^{-1}).[10] Moreover, the electrical conductivity is even better than that of titanium commonly used as electrode. We repeated measurements of electrical conductivity on more than 30 devices and found that all devices show similar results. Given that $PtTe_2$ single crystals have such a large electrical conductivity and atomically smooth surface, it may be used as electrode for 2D semiconducting materials to improve contact properties.[15,48] Note that all the measurements of electrical conductivity were done at room
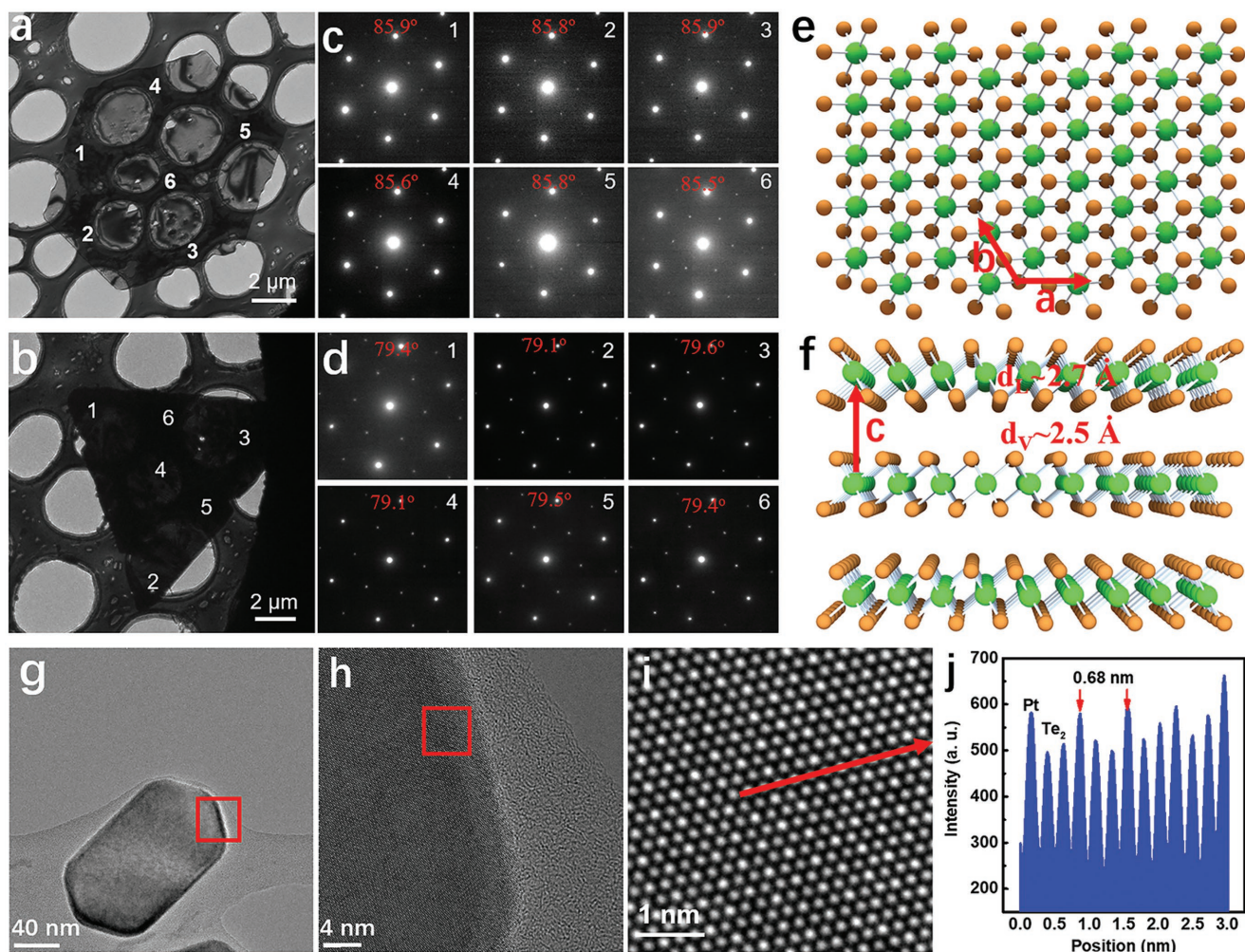
Figure 3. TEM characterizations of the as-grown PtTe$_2$ single crystals. The low-magnification TEM images of a) hexagonal and b) triangular PtTe$_2$ flakes and c,d) their corresponding SAED patterns taken from the points labeled with numbers 1–6, respectively. The angles of dashed lines linking the near vertical two dots with respect to the horizontal lines are marked in the corresponding patterns. e,f) Top- and side-view structural models of PtTe$_2$ single crystal (Pt atoms, green; Te atoms, brown). g–i) The lower magnification of g) PtTe$_2$ nanosheet and corresponding zoomed-in h) higher magnification and i) atomic-resolution TEM images highlighted by red rectangles. j) Intensity line profile extracted along the red solid line in (i).
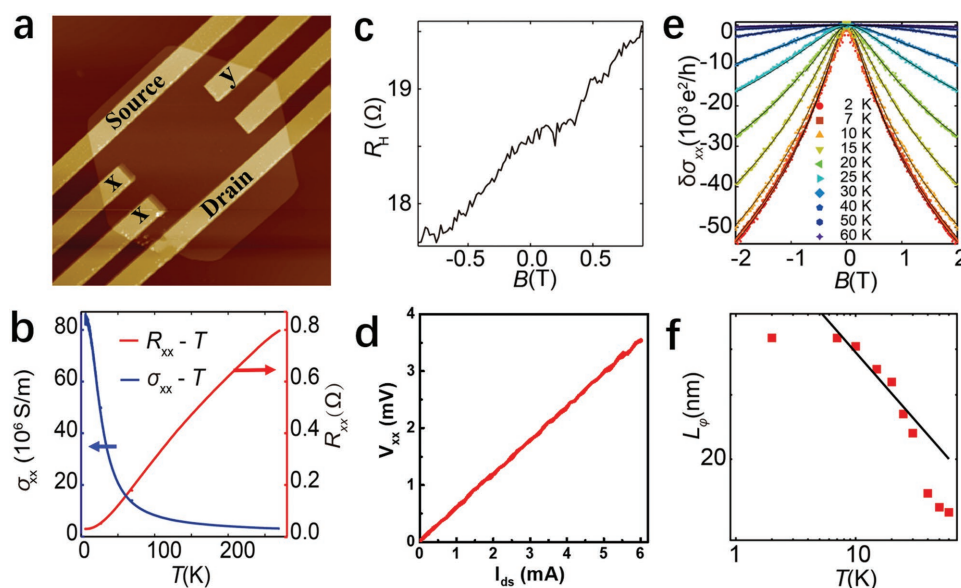
temperature. At low temperature, electrical conductivity of PtTe$_2$ is strongly dependent on specific scattering mechanisms.

To investigate how electron scattering mechanisms affect electrical conductivity of PtTe$_2$ at low temperatures, we carried out the measurement of four-terminal electrical transport in an He^4 cryostat at various magnetic fields. Interestingly, we observe that the perpendicular magnetic field dependence of magnetoconductivity of PtTe$_2$ exhibits a weak antilocalization (WAL) behavior (see Figure 4e), which persists up to 60 K and becomes much more prominent at lower temperature. The WAL effect can be manifested by the quantum interference induced change in electrical conductivity of diffusive regime. Besides, the presence of WAL effect is an indication of strong spin-orbit coupling in PtTe$_2$, which is consistent with the fact that heavy transition metal element Pt leads to a strong spin-orbit interaction in PtTe$_2$. In the limit of strong spin-orbit coupling, we fitted the experimental data of magneto-conductance (defined as $\delta\sigma_{xx}(H) = (L/WH)/R_{xx}(H) - (L/WH)/R_{xx}(0)$) using Hikami–Larkin–Nagaoka (HLN) model[49]

$$\Delta\sigma(B) = \frac{ae^2}{\pi h}\left\{\left[\ln\left(\frac{B_\varnothing}{B}\right) - \Psi\left(\frac{1}{2} + \frac{B_\varnothing}{B}\right)\right]\right\} \quad (1)$$

where e is the elementary charge, h is the Planck constant, ψ is the digamma function, and B_φ refers to the characteristic field of phase coherence. As shown in Figure 4e, the HLN theory (solid lines) agrees well with experimental data (symbols). Similar to the previous reports, α is much larger than that in 2D systems due to bulk effect.[50,51] Through the fittings, we extracted the corresponding phase decoherence length $l_\varphi = \sqrt{h/(8\pi eB_\varphi)}$, with results shown in Figure 4f. It is found that l_φ displays a $T^{-\gamma}$ dependence with $\gamma = 0.37 \pm 0.05$ within temperature ranges from $T = 7$ to 30 K. The extracted value of γ indicates that electron dephasing in PtTe$_2$ at low temperatures may be attributed to electron-electron interactions ($\gamma = 0.5$), rather than the electron-phonon interactions ($\gamma = 1$).

Physical properties of 2D materials are strongly dependent on their thickness, especially for group-10 TMD materials with strong interlayer interactions.[26,29] To obtain atomically thin

**ADVANCED
SCIENCE NEWS**

www.advancedsciencenews.com

**ADVANCED
FUNCTIONAL
MATERIALS**

www.afm-journal.de

Figure 4. The electrical transport of SLS-grown PtTe$_2$ single crystal device. a) The AFM topography image of a PtTe$_2$ Hall bar single crystal device. b) R_{xx}–T and the corresponding σ_{xx}–T curves. $\sigma_{xx} = (L/WH)/R_{xx}$, where L, W, and H are the length, width, and thickness of the channel, respectively. c) The hall R_{xy}–B curve. d) V_{xx}–I_{ds} characteristic curve. e) The temperature-dependent magnetoconductivity $\delta\sigma_{xx}(B)$–B. The symbols represent experimental data and solid lines are theoretical results based on Equation (1). f) The extracted dephasing length L_φ versus T shows a power-law rule of $T^{-\gamma}$ (the black solid line) with the $\gamma = 0.37 \pm 0.05$.

samples, mechanical exfoliation and CVD methods are usually used. However strong interlayer interactions and high melting-point transition metal pose challenges for obtaining atomically thin PtTe$_2$. Here a simple and general approach was developed to obtain the atomically thin PtTe$_2$ with controlled thickness. We thinned as-synthesized bulk PtTe$_2$ single crystals down to atomic thickness by utilizing an argon plasma ion beam etching (IBE) method, as displayed in **Figure 5**a–d. When argon plasma is switched on, the relative light Te atoms at the top surface would be removed (see Figure 5b), leaving many Te vacancies. With plasma bombardment of longer time, heavy Pt atoms at the top surface would be also removed, leading to removal of PtTe$_2$ uni-layer (see Figure 5c). Eventually, atomically thin PtTe$_2$ single crystals can be obtained (see Figure 5d).

The obtained atomically thin PtTe$_2$ crystals through argon plasma IBE method still retain high crystallinity. Figure 5e shows an optical microscopy image of a plasma-thinned

Table 1. Comparison of the electrical conductivity for SLS-grown PtTe$_2$ single crystal, several 2D metallic materials, and conventional metals.

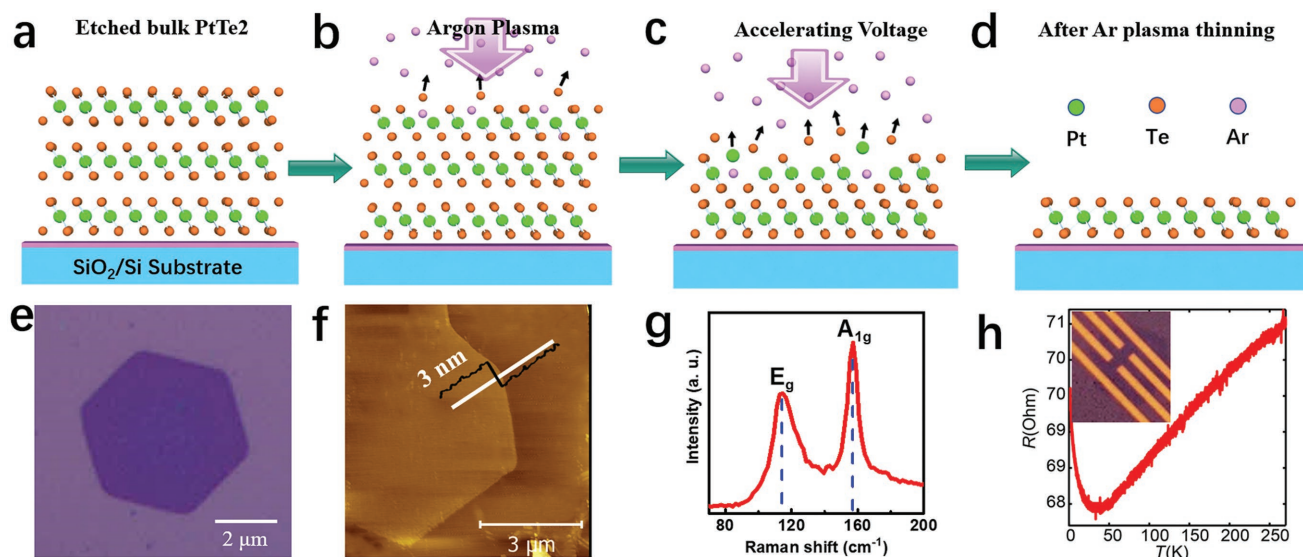| Different materials	Conductivity [S m^{-1}]	References
1T-MoS$_2$	$1.0–10 \times 10^3$	[52]
rGO	1.0×10^4	[53]
Graphene	$0.2–2.0 \times 10^6$	[54–56]
CVD-VS$_2$	3.0×10^5	[15]
CVD-VSe$_2$	1.1×10^6	[10]
Stainless Steel	1.4×10^6	[57]
Titanium	2.4×10^6	[58]
PtTe$_2$	3.3×10^6	This work
Gold	4.1×10^7	[59]

equilateral hexagonal-shape sample with identical color contrast, which is primarily assigned to single crystalline PtTe$_2$ with uniform thickness. Surface roughness of less than 0.5 nm in the height profile indicates that the thinning approach of using argon plasma does not destroy its crystallinity and that few of PtTe$_2$ traces are left in the surface. We note that similar approach has been applied for bulk samples with weak inter-layer interaction to obtain thin flakes, such as MoS$_2$ layer thinning with a local anodic oxidation method.[60–62] Different from prior works, we modified IBE instrument to speed up argon plasma and successfully thinned as-grown PtTe$_2$ with strong interlayer interaction down to atomically thin crystals. To obtain high-quality PtTe$_2$ flakes through thinning approach, we carefully controlled the energy of argon plasma as small as possible by adjusting the accelerating voltage.

To further examine the crystallinity of post-thinning PtTe$_2$, we performed Raman spectroscopy and Raman mapping on the samples. Raman spectrum in Figure 5g shows two prominent E$_g$ and A$_{1g}$ modes centered at ≈116.7 and ≈157.0 cm^{-1}, consistent with that of pre-thinned PtTe$_2$ crystals. As expected, we find that the E$_g$ mode has blue-shift of 6.7 cm^{-1} compared to as-synthesized bulk ones, due to strong interlayer interactions.[63,64] The full width at half maximum (FWHM) of A$_{1g}$ peak is not sensitive to the variation in thickness of PtTe$_2$, therefore it could be used as a criteria to evaluate the quality of plasma-thinned PtTe$_2$ single crystals.[65] The FWHM of A$_{1g}$ mode is 6.9 cm^{-1} and is close to as-synthesized bulk one (6.7 cm^{-1}), thus providing a further proof of high-quality PtTe$_2$ crystal after etching. To examine the change in electrical conductivity, we fabricated a Hall bar device (see the inset in Figure 5h) based on thinned PtTe$_2$ flake. Measurement of electric transport (see Figure 5h) demonstrates that thinned samples still retain a superior electrical conductivity (0.43×10^6 S m^{-1}),

**ADVANCED
SCIENCE NEWS**
www.advancedsciencenews.com

**ADVANCED
FUNCTIONAL
MATERIALS**
www.afm-journal.de

Figure 5. a–d) Schematic showing the processes of layer-by-layer thinning of bulk PtTe$_2$ single crystals by accelerated argon plasma. e,f) Optical microscopy and AFM topography images of PtTe$_2$ single crystal after argon plasma thinning, respectively. The inserted height profile extracted along the white solid line in (f) gives a thickness of ≈3 nm. g) Raman spectrum of PtTe$_2$ flake after argon plasma thinning. h) Temperature–dependent resistivity for the thinned PtTe$_2$ device. The inset shows a typical Hall bar device fabricated with a hexagonal thinned PtTe$_2$.

which suggests a huge potential of plasma etching technique in thinning layered materials with strong-interlayer interactions.

3. Conclusion

In summary, we realize the first low-temperature eutectic liquid-phase synthesis of high-quality PtTe$_2$ single crystals with thickness ranging from 2 to 200 nm in an ambient-pressure CVD system. The growth mechanism is based on SLS eutectic solidification, which is completely different from conventional high-temperature gas-phase synthesis of TMDs. We find that the electrical conductivity of as-grown PtTe$_2$ is superior to all metallic TMDs ever reported. We also experimentally identify the weak antilocalization phenomenon in type-II Dirac semimetal for the first time. Furthermore, we develop a simple and general strategy of obtaining atomically thin PtTe$_2$ samples with controllable thickness by lay-by-layer thinning as-grown samples, which can still retain high crystallinity and exhibits excellent electrical conductivity. The approaches reported in this paper open up a new avenue for the controllable growth and fabrication of TMD materials with high melting-point transition metal and strong interlayer interactions and pave the way for realizing novel optoelectronic and topological electronics based on 2D TMD materials.

4. Experimental Section

Material Synthesis: Tellurium (Te, Sigma-Aldrich, 4N purity) powders and platinum (Pt, Sputtering target, 5N purity) films were used as the reactant precursors to synthesize PtTe$_2$ single crystals on SiO$_2$/Si substrates in the CVD-like furnace. The Ar/H$_2$ mixture was used as the carrier gas to carry Te vapor from the substrates to downstream. In a typical procedure of PtTe$_2$ growth, Pt films with various thicknesses (from 0.2 to 1.5 nm) were first deposited onto SiO$_2$/Si substrates as Pt

reactant precursor using electron beam evaporation. Excess Te powder with different weight (from 50 to 200 mg) was uniformly dispersed on the top of the as-deposited Pt films. The synthesis processes were done in the CVD-like quartz tube with 1 inch diameter under ambient pressure. Upon pumping, the Ar/H$_2$ mixed gas flow at 500 sccm was introduced to purge air from the quartz tube for 20 min, and then gas flow was maintained at 200 sccm during growth. The furnace was heated to 500 °C in 20 min, and then heated up to 700 °C in 30 min, followed by cooling down to 500 °C in 30 min controlled by a proportion integration differentiation controller. Finally, the furnace was naturally cooled down to room temperature with keeping Ar/H$_2$ gas flow and then switched off.

Sample Transfer and TEM Characterization: Polymethyl-methacrylate (PMMA) was spin-coated on the as-grown PtTe$_2$ flakes on SiO$_2$/Si substrates, and then PMMA/ PtTe$_2$ stack was transferred onto a TEM grid by etching SiO$_2$ in NaOH (2 M) solution. Lastly, PMMA was removed by acetone and isopropanol. High-resolution TEM (Titan 80–300) and SAED were performed at the accelerating voltage of 200 kV.

Material Characterizations: X-ray photoelectron spectroscopy was performed on a PHI 5000 Versaprobe system using AL Kα as X-ray source. The composition and elements distribution of as-synthesized flakes were determined by EDS attached to the scanning electron microscope (SEM, FEI Quanta 200 ESEM). The atomic force microscopy measurements (Bruker multimode 8) were performed by using ScanAsyst mode. Raman spectroscopy/mappings were carried out under a 532.0 nm laser light and silicon-based CCD detector at room temperature using HORIBA JOBIN YVON HR800 Raman system. The spectra were calibrated by 520.7 cm^{-1} phonon mode from the silicon substrate. XRD was used to measure the structural information of PtTe$_2$ crystals (Rigaku D/Max RAPID-ǁ with Mo Kα radiation, Japan).

Device Fabrication and Electrical Measurements: A standard electron-beam lithography method was used to pattern (FEI F50 with Raith pattern generation system) electrodes. Ti/Au electrodes (5 nm/100 nm) were deposited via standard electron-beam evaporation. The I_{ds}–V_{ds} curves of four-probe planar devices were measured by an Agilent B1500A semiconductor analyzer connected to a probe station at room temperature.

Materials Thinning: A commercial ion-beam etching instrument (Advanced IBE-150) with a Kaufmann ion source was utilized to thin as-grown PtTe$_2$ single crystals. The target holder was water-cooled and rotated at a constant velocity to ensure uniform etching. The base

pressure was set to be higher than 8×10^{-4} Pa before introducing the argon flow, and then maintained at 2×10^{-2} Pa during etching process. Argon plasma with acceleration power of 90 eV was used with various current densities and irradiation time at room temperature.

Supporting Information

Supporting Information is available from the Wiley Online Library or from the author.

Conflict of Interest

The authors declare no conflict of interest.

[1] S. Z. Butler, S. M. Hollen, L. Y. Cao, Y. Cui, J. A. Gupta, H. R. Gutierrez, T. F. Heinz, S. S. Hong, J. X. Huang, A. F. Ismach, E. Johnston-Halperin, M. Kuno, V. V. Plashnitsa, R. D. Robinson, R. S. Ruoff, S. Salahuddin, J. Shan, L. Shi, M. G. Spencer, M. Terrones, W. Windl, J. E. Goldberger, *ACS Nano* **2013**, *7*, 2898.

[2] Q. Ji, Y. Zhang, Y. Zhang, Z. Liu, *Chem. Soc. Rev.* **2015**, *44*, 2587.

[3] Y. Shi, H. Li, L. J. Li, *Chem. Soc. Rev.* **2015**, *44*, 2744.

[4] Z. Zhang, P. Chen, X. Duan, K. Zang, J. Luo, X. Duan, *Science* **2017**, *357*, 788.

[5] T. Yang, B. Zheng, Z. Wang, T. Xu, C. Pan, J. Zou, X. Zhang, Z. Qi, H. Liu, Y. Feng, W. Hu, F. Miao, L. Sun, X. Duan, A. Pan, *Nat. Commun.* **2017**, *8*, 1906.

[6] X. Li, L. Tao, Z. Chen, H. Fang, X. Li, X. Wang, J.-B. Xu, H. Zhu, *Appl. Phys. Rev.* **2017**, *4*, 021306.

[7] Q. H. Wang, K. Kalantar-Zadeh, A. Kis, J. N. Coleman, M. S. Strano, *Nat. Nanotechnol.* **2012**, *7*, 699.

[8] M. Chhowalla, H. S. Shin, G. Eda, L. J. Li, K. P. Loh, H. Zhang, *Nat. Chem.* **2013**, *5*, 263.

[9] H. Wang, Y. Chen, M. Duchamp, Q. Zeng, X. Wang, S. H. Tsang, H. Li, L. Jing, T. Yu, E. H. T. Teo, Z. Liu, *Adv. Mater.* **2018**, *30*, 1704382.

[10] Z. Zhang, J. Niu, P. Yang, Y. Gong, Q. Ji, J. Shi, Q. Fang, S. Jiang, H. Li, X. Zhou, L. Gu, X. Wu, Y. Zhang, *Adv. Mater.* **2017**, *29*, 1702359.

[11] L. Cao, *MRS Bull.* **2015**, *40*, 592.

[12] C. Xu, L. Wang, Z. Liu, L. Chen, J. Guo, N. Kang, X. L. Ma, H. M. Cheng, W. Ren, *Nat. Mater.* **2015**, *14*, 1135.

[13] Y. Fu, E. Liu, H. Yuan, P. Tang, B. Lian, G. Xu, J. Zeng, Z. Chen, Y. Wang, W. Zhou, K. Xu, A. Gao, C. Pan, M. Wang, B. Wang, S.-C. Zhang, Y. Cui, H. Y. Hwang, F. Miao, *Npj Quantum Mater.* **2017**, *2*, 52.

[14] R. Kappera, D. Voiry, S. E. Yalcin, B. Branch, G. Gupta, A. D. Mohite, M. Chhowalla, *Nat. Mater.* **2014**, *13*, 1128.

[15] Q. Ji, C. Li, J. Wang, J. Niu, Y. Gong, Z. Zhang, Q. Fang, Y. Zhang, J. Shi, L. Liao, X. Wu, L. Gu, Z. Liu, Y. Zhang, *Nano Lett.* **2017**, *17*, 4908.

[16] J. Shi, X. Wang, S. Zhang, L. Xiao, Y. Huan, Y. Gong, Z. Zhang, Y. Li, X. Zhou, M. Hong, Q. Fang, Q. Zhang, X. Liu, L. Gu, Z. Liu, Y. Zhang, *Nat. Commun.* **2017**, *8*, 958.

[17] C. Tan, Z. Luo, A. Chaturvedi, Y. Cai, Y. Du, Y. Gong, Y. Huang, Z. Lai, X. Zhang, L. Zheng, X. Qi, M. H. Goh, J. Wang, S. Han, X. J. Wu, L. Gu, C. Kloc, H. Zhang, *Adv. Mater.* **2018**, *30*, 1705509.

[18] Q. Zhang, W. Wang, J. Zhang, X. Zhu, Q. Zhang, Y. Zhang, Z. Ren, S. Song, J. Wang, Z. Ying, R. Wang, X. Qiu, T. Peng, L. Fu, *Adv. Mater.* **2018**, e1707123.

[19] A. Politano, G. Chiarello, C.-N. Kuo, C. S. Lue, R. Edla, P. Torelli, V. Pellegrini, D. W. Boukhvalov, *Adv. Funct. Mater.* **2018**, *28*, 1706504.

[20] M. Yan, H. Huang, K. Zhang, E. Wang, W. Yao, K. Deng, G. Wan, H. Zhang, M. Arita, H. Yang, Z. Sun, H. Yao, Y. Wu, S. Fan, W. Duan, S. Zhou, *Nat. Commun.* **2017**, *8*, 257.

[21] A. A. Soluyanov, D. Gresch, Z. Wang, Q. Wu, M. Troyer, X. Dai, B. A. Bernevig, *Nature* **2015**, *527*, 495.

[22] Y. Wang, E. Liu, H. Liu, Y. Pan, L. Zhang, J. Zeng, Y. Fu, M. Wang, K. Xu, Z. Huang, Z. Wang, H. Z. Lu, D. Xing, B. Wang, X. Wan, F. Miao, *Nat. Commun.* **2016**, *7*, 13142.

[23] L. Huang, T. M. McCormick, M. Ochi, Z. Zhao, M.-T. Suzuki, R. Arita, Y. Wu, D. Mou, H. Cao, J. Yan, N. Trivedi, A. Kaminski, *Nat. Mater.* **2016**, *15*, 1155.

[24] K. Deng, G. Wan, P. Deng, K. Zhang, S. Ding, E. Wang, M. Yan, H. Huang, H. Zhang, Z. Xu, J. Denlinger, A. Fedorov, H. Yang, W. Duan, H. Yao, Y. Wu, S. Fan, H. Zhang, X. Chen, S. Zhou, *Nat. Phys.* **2016**, *12*, 1105.

[25] D. Dai, H. J. Koo, M. H. Whangbo, C. Soulard, X. Rocquefelte, S. Jobic, *J. Solid State Chem.* **2003**, *173*, 114.

[26] Y. Zhao, J. Qiao, P. Yu, Z. Hu, Z. Lin, S. P. Lau, Z. Liu, W. Ji, Y. Chai, *Adv. Mater.* **2016**, *28*, 2399.

[27] Z. Wang, Q. Li, F. Besenbacher, M. Dong, *Adv. Mater.* **2016**, *28*, 10224.

[28] Y. Wang, L. Li, W. Yao, S. Song, J. T. Sun, J. Pan, X. Ren, C. Li, E. Okunishi, Y. Q. Wang, E. Wang, Y. Shao, Y. Y. Zhang, H. T. Yang, E. F. Schwier, H. Iwasawa, K. Shimada, M. Taniguchi, Z. Cheng, S. Zhou, S. Du, S. J. Pennycook, S. T. Pantelides, H. J. Gao, *Nano Lett.* **2015**, *15*, 4013.

[29] A. Ciarrocchi, A. Avsar, D. Ovchinnikov, A. Kis, *Nat. Commun.* **2018**, *9*, 919.

[30] S. Soled, A. Wold, O. Gorochov, *Mater. Res. Bull.* **1975**, *10*, 831.

[31] J. Mangin, P. Veber, *J. Cryst. Growth* **2008**, *310*, 3077.

[32] E. I. Givargizov, *J. Cryst. Growth* **1975**, *31*, 20.

[33] Y. Gong, Z. Lin, G. Ye, G. Shi, S. Feng, Y. Lei, A. L. Elias, N. Perea-Lopez, R. Vajtai, H. Terrones, Z. Liu, M. Terrones, P. M. Ajayan, *ACS Nano* **2015**, *9*, 11658.

[34] Y. Gong, J. Lin, X. Wang, G. Shi, S. Lei, Z. Lin, X. Zou, G. Ye, R. Vajtai, B. I. Yakobson, H. Terrones, M. Terrones, B. K. Tay, J. Lou, S. T. Pantelides, Z. Liu, W. Zhou, P. M. Ajayan, *Nat. Mater.* **2014**, *13*, 1135.

[35] I. Song, C. Park, M. Hong, J. Baik, H. J. Shin, H. C. Choi, *Ange. Chem.* **2014**, *53*, 1266.

[36] J. Zhou, J. Lin, X. Huang, Y. Zhou, Y. Chen, J. Xia, H. Wang, Y. Xie, H. Yu, J. Lei, D. Wu, F. Liu, Q. Fu, Q. Zeng, C.-H. Hsu, C. Yang, L. Lu, T. Yu, Z. Shen, H. Lin, B. I. Yakobson, Q. Liu, K. Suenaga, G. Liu, Z. Liu, *Nature* **2018**, *556*, 355.

[37] L. Zhang, C. Wang, X. L. Liu, T. Xu, M. Long, E. Liu, C. Pan, G. Su, J. Zeng, Y. Fu, Y. Wang, Z. Yan, A. Gao, K. Xu, P. H. Tan, L. Sun, Z. Wang, X. Cui, F. Miao, *Nanoscale* **2017**, *9*, 19124.

[38] Q. Wang, K. Xu, Z. Wang, F. Wang, Y. Huang, M. Safdar, X. Zhan, F. Wang, Z. Cheng, J. He, *Nano Lett.* **2015**, *15*, 1183.

[39] A. Kjekshus, F. Gronvold, *Acta Chem. Scand.* **1959**, *13*, 1767.

[40] L. Li, W. Wang, P. Gong, X. Zhu, B. Deng, X. Shi, G. Gao, H. Li, T. Zhai, *Adv. Mater.* **2018**, *30*, 1706331.

[41] J. Wu, N. Mao, L. Xie, H. Xu, J. Zhang, *Ange. Chem.* **2015**, *54*, 2366.

[42] N. A. Lanzillo, A. Glen Birdwell, M. Amani, F. J. Crowne, P. B. Shah, S. Najmaei, Z. Liu, P. M. Ajayan, J. Lou, M. Dubey, S. K. Nayak, T. P. O'Regan, *Appl. Phys. Lett.* **2013**, *103*, 093102.

[43] M. Thripuranthaka, D. J. Late, *ACS Appl. Mater. Interfaces* **2014**, *6*, 1158.

[44] D. J. Late, *ACS Appl. Mater. Interfaces* **2015**, *7*, 5857.

[45] A. S. Pawbake, M. S. Pawar, S. R. Jadkar, D. J. Late, *Nanoscale* **2016**, *8*, 3008.

[46] Y. Zhan, Z. Liu, S. Najmaei, P. M. Ajayan, J. Lou, *Small* **2012**, *8*, 966.

[47] F. Gronvold, H. Haraldsen, A. Kjekshus, *Acta Chem. Scand.* **1960**, *14*, 1879.

[48] Y. Liu, P. Stradins, S.-H. Wei, *Sci. Adv.* **2016**, *2*, e1600069.

[49] S. Hikami, A. I. Larkin, Y. Nagaoka, *Prog. Theor. Phys.* **1980**, *63*, 707.

[50] N. P. Butch, P. Syers, K. Kirshenbaum, A. P. Hope, J. Paglione, *Phys. Rev. B* **2011**, *84*, 220504.

[51] Z. Hou, Y. Wang, E. Liu, H. Zhang, W. Wang, G. Wu, *Appl. Phys. Lett.* **2015**, *107*, 202103.

[52] M. Acerce, D. Voiry, M. Chhowalla, *Nat. Nanotechnol.* **2015**, *10*, 313.

[53] Y. Zhu, S. Murali, W. Cai, X. Li, J. W. Suk, J. R. Potts, R. S. Ruoff, *Adv. Mater.* **2010**, *22*, 3906.

[54] Z. S. Wu, W. C. Ren, L. B. Gao, J. P. Zhao, Z. P. Chen, B. L. Liu, D. M. Tang, B. Yu, C. B. Jiang, H. M. Cheng, *ACS Nano* **2009**, *3*, 411.

[55] R. Raccichini, A. Varzi, S. Passerini, B. Scrosati, *Nat. Mater.* **2015**, *14*, 271.

[56] Y. Hao, L. Wang, Y. Liu, H. Chen, X. Wang, C. Tan, S. Nie, J. W. Suk, T. Jiang, T. Liang, J. Xiao, W. Ye, C. R. Dean, B. I. Yakobson, K. F. McCarty, P. Kim, J. Hone, L. Colombo, R. S. Ruoff, *Nat. Nanotechnol.* **2016**, *11*, 426.

[57] R. P. Tye, *Mech. Eng.* **1973**, *95*, 66.

[58] O. Umezawa, K. Ishikawa, *Cryogenics* **1992**, *32*, 873.

[59] R. A. Matula, *J. Phys. Chem. Ref. Data* **1979**, *8*, 1147.

[60] Y. L. Liu, H. Y. Nan, X. Wu, W. Pan, W. H. Wang, J. Bai, W. W. Zhao, L. T. Sun, X. R. Wang, Z. H. Ni, *ACS Nano* **2013**, *7*, 4202.

[61] W. Lu, H. Nan, J. Hong, Y. Chen, C. Zhu, Z. Liang, X. Ma, Z. Ni, C. Jin, Z. Zhang, *Nano Res.* **2014**, *7*, 853.

[62] M. Donarelli, F. Perrozzi, F. Bisti, F. Paparella, V. Feyer, A. Ponzoni, M. Gonchigsuren, L. Ottaviano, *Nanoscale* **2015**, *7*, 11453.

[63] H. Li, Q. Zhang, C. C. R. Yap, B. K. Tay, T. H. T. Edwin, A. Olivier, D. Baillargeat, *Adv. Funct. Mater.* **2012**, *22*, 1385.

[64] C. Lee, H. Yan, L. E. Brus, T. F. Heinz, J. Hone, S. Ryu, *ACS Nano* **2010**, *4*, 2695.

[65] X. Wang, H. Feng, Y. Wu, L. Jiao, *J. Am. Chem. Soc.* **2013**, *135*, 5304.

1803746 (9 of 9)